Journal of Porous Materials (2026) 33:33–51
https://doi.org/10.1007/s10934-025-01846-2

Thermo-kinetic characterization and performance evaluation of Fe_3O_4@activated carbon for gas-phase PAH adsorption

Kaan Isinkaralar[1] · Aydin Turkyilmaz[1] · Huseyin Guran Unal[2] · Chander Prakash[3] · Ahmad Hosseini-Bandegharaei[4,5,6] · Antonio Cannuli[7]

Received: 26 June 2025 / Accepted: 16 August 2025 / Published online: 3 October 2025

Abstract

Acenaphthene (ACE), a pervasive ambient air pollutant, constitutes considerable health threats even at low concentrations. Although carbonaceous materials are commonly utilized for ACE remediation, their efficiency is still debated with experiments showing their effects under different conditions. The mechanisms explaining these seemingly contradictory observations are not fully understood, limiting the development of adsorbents with stable and predictable performance under varying thermos-hygrometric conditions. To address this gap, we synthesized a material featuring a tailored morphology, mesoporous architecture, and rich surface functionalization, and we carried out an extensive characterization using SEM, BET, FTIR, VSM, and XRD techniques to quantify structural, thermal, and magnetic properties. The Fe_3O_4 nanoparticles-functionalized activated carbon (BG-AC@NPs) demonstrated a high gas-phase ACE removal efficiency of 99.7% under controlled adsorption conditions, and the equilibrium was stabilized within 40 min, with a maximum adsorption capacity (BG-AC@NPs) of 378.3 mg/g. Adsorption kinetics were precisely fitted through the use of a pseudo-second-order (PSO) model, which gave an R^2 coefficient higher than 0.940. Moreover, the Langmuir model provided a good representation of the adsorption isotherms and the R^2 value is >0.988, indicating the occurrence of monolayer adsorption. Thermodynamic analysis indicated a positive ΔH° (51.354 kJ/mol) and ΔS° (0.024 J/mol K), together with a negative ΔG°, it verifies the spontaneous, endothermic nature of adsorption with enhanced randomness. Notably, BG-AC@NPs retained over 80% efficiency after multiple regeneration cycles. This study advances gas-phase adsorption systems by integrating material design and thermal-kinetic measurement strategies. Furthermore, it highlights how solid-gas clustering phenomena at pore inlets influence adsorption kinetics even at optimum levels, guiding the optimization of pore structure and surface chemistry for high-performance PAHs capture.

✉ Kaan Isinkaralar
kisinkaralar@kastamonu.edu.tr

Antonio Cannuli
antonio.cannuli@unime.it

[1] Department of Environmental Engineering, Faculty of Engineering and Architecture, Kastamonu University, Kastamonu 37150, Türkiye

[2] Department of Mechanical Engineering, Faculty of Engineering and Architecture, Kastamonu University, Kastamonu 37150, Türkiye

[3] School of Engineering and Technology, Sanskaram University, Jhajjar 124108, Haryana, India

[4] Research and Innovation Cell, Rayat Bahra University, Mohali, Punjab, India

[5] Department of Chemistry, Semnan University, Semnan, Iran

[6] Department of Sustainable Engineering, Saveetha School of Engineering, SIMATS, Chennai 602105, Tamil Nadu, India

[7] Department of Engineering, University of Messina, C.da di Dio, Messina 98166, Italy

Graphical abstract

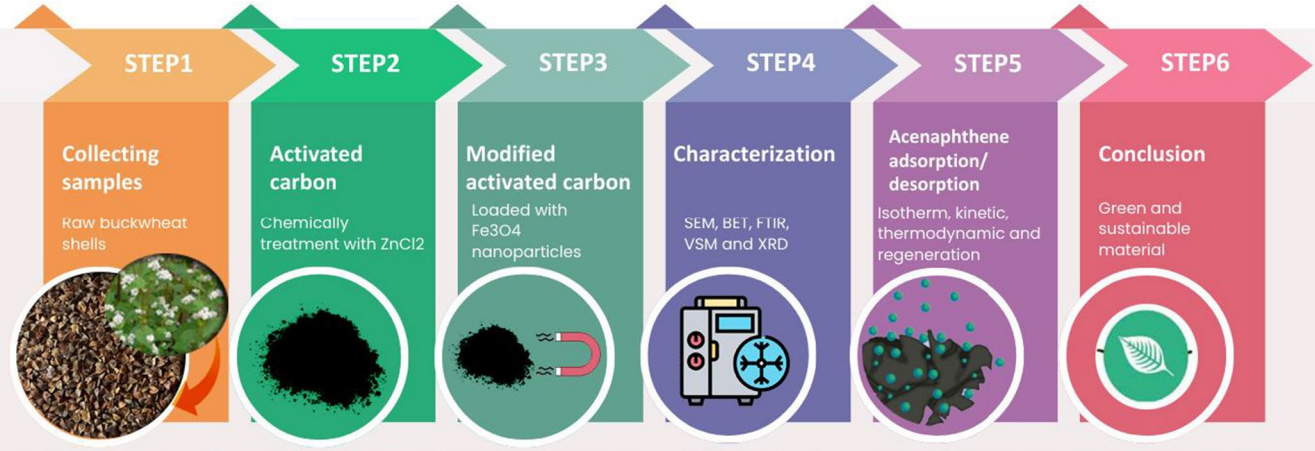

Highlights

- BG-AC and BG-AC@NPs were synthesized and characterized for gas ACE adsorption.
- BG-AC@NPs showed a superior ACE removal efficiency of 99.7% under optimal conditions.
- Langmuir model defined the adsorption process with a 378.3 mg/g capacity.
- Pseudo-second-order model was most suitable for fitting the kinetic results.
- BG-AC@NPs maintained over 80% efficiency even after multiple regeneration cycles.

Keywords Nanocomposite · Thermo-kinetic characterization · Isotherms and kinetic studies · Environmental metrology · Advanced measurement techniques

1 Introduction

Poor air quality resulting from hazardous airborne pollutants represents a major global environmental issue, especially in urban areas. Gaseous and particulate-bound contaminants originating from human activities release a variety of harmful substances—such as dyes, fatliquoring agents, and tannins, that are difficult to remove effectively [1]. Among the most concerning pollutants are polycyclic aromatic hydrocarbons (PAHs), which are mainly created through the deficient burning of fossil fuels and biomass [2]. In this context, acenaphthene (ACE) is frequently detected in urban air and is characterized by a complex chemical structure and persistent behavior [3]. ACE, a tricyclic member of the PAH family, is known for its mutagenic and carcinogenic effects [4]. It is commonly emitted through industrial waste gases, vehicle exhaust, and residential heating systems using biomass or coal [5]. These emissions and atmospheric variables contribute to its widespread presence in indoor and outdoor air and complicate its removal.

Meanwhile, the significant increase in agricultural and forestry activities has resulted in the formation of large volumes of biomass waste [6, 7], which—if not properly managed—can negatively impact environmental and human health [8]. Biomass residues are often disposed of inefficiently, through open-air burning or landfill accumulation, which contribute to greenhouse gas emissions and air quality deterioration [9, 10]. Consequently, the valorization of agro-waste into functional materials, such as activated carbons, is gaining interest as a sustainable remediation approach [11, 12].

Among pollutant abatement techniques, adsorption using carbonaceous materials is widely recognized for its efficiency in removing both oxygenated (OPAHs) and nitrated (NPAHs) derivatives of PAHs under various environmental conditions [13]. However, the performance of these materials is known to vary under indoor conditions—affected by parameters such as humidity, temperature, and molecular weight of the target compound [14, 15]. Increased temperature may enhance gas-phase PAH concentration and radical reactivity. Still, it may also alter adsorption kinetics due to atmospheric oxidation [16] and pore diffusion limitations [17].

Although traditional separation methods like oxidation, ion exchange, and photolysis are available, they often suffer from high energy demand and operational complexity, making them unsuitable for low-cost, small-scale applications [18]. Alternatives such as pressure swing adsorption and membrane separation have been developed; these too face challenges in selectivity and long-term stability [19]. As such, adsorption remains the most promising strategy,

particularly when using tunable materials like nanostructured carbons and composites [20–22]. Metal oxide nanoparticles (M-NPs), particularly iron oxide (Fe_3O_4), have gained attention in nanotechnology applications due to their large surface area [23, 24], magnetic properties, low toxicity, and compatibility with activated carbon supports [25, 26]. Yet, standalone IONPs Fe_3O_4, have gained attention in nanotechnology applications due to their enhanced properties [27–29]. Various studies have examined the effectiveness of Fe_3O_4/AC composites for adsorption of dyes and pollutants from water [30–32], showing that physico-chemical properties and synthesis temperature significantly influence performance. Fe_3O_4 exhibits remarkable surface activities that translate into significant adsorption capabilities, making it valuable in removing pollutants from aqueous solutions [33]. Their nanoscale size and high surface area amplify these properties, positioning them as effective sorbents for dissolved metals and organic dyes [34]. Integrating Fe_3O_4 and hydroxides with nanomaterials and polymers enhances their versatility in removing heavy metals and organic pollutants, offering a promising avenue for sustainable wastewater treatment [35]. Understanding Fe_3O_4's involvement in the adsorption role requires investigating the types of adsorption and the mechanisms governing these interactions (physisorption vs. chemisorption), and the potential of Fe_3O_4 in adsorbent regeneration [36].

This study focuses on synthesizing, characterizing, and evaluating a Fe_3O_4-functionalized activated carbon (BG-AC@NPs) derived from buckwheat husks to remove gas-phase ACE. Characterization techniques including BET, XRD, SEM, VSM, and FTIR were employed to analyze surface area, porosity, magnetic behavior, and chemical functionality. The adsorption performance was evaluated under varying thermal and environmental conditions to understand better ACE adsorption's kinetic, thermodynamic, and mechanistic aspects. Through this integrated approach, we aim to contribute new insights for designing high-performance adsorbents optimized for gas-phase PAH removal, with potential applications in indoor air purification and environmental monitoring systems.

2 Materials and methods

2.1 Reagents and raw biomass materials

Raw agricultural waste from buckwheat grain husks (BGHW, *Fagopyrum esculentum* Moench), was employed as a low-cost and sustainable carbon precursor. The BGHW was collected from a local buckwheat processing facility in Kastamonu, Türkiye. The biomass was washed with deionized water, air-dried in air at room temperature and then kept in a desiccator before handling. The chemical activating agent used was zinc chloride ($ZnCl_2$, 98%), while iron(III) nitrate hexahydrate ($Fe(NO_3)_3.9H_2O$, ≥98%) served as the magnetic precursor. Citric acid ($C_6H_8O_7$, (≥99.7%) and ethanol (C_2H_6O, ≥99%,) were employed as complexing agents and solvents during the impregnation and functionalization steps. Hydrochloric acid (HCl) and sodium hydroxide (NaOH) solutions were adjusted pH levels. The model contaminant used for adsorption studies was acenaphthene (ACE) ($C_{12}H_{10}$, ≥ 96%), selected due to its relevance as a representative polycyclic aromatic hydrocarbon (PAH) commonly found in atmospheric particulate matter (PM). All chemical reagents were of analytical grade and supplied by Merck (Germany). Deionized water (resistivity≥18.2 MΩ·cm) was used throughout all preparation and experimental procedures to ensure reproducibility and minimize contamination.

2.2 Synthesis and functionalization procedures

The activated carbon (BG-AC) was synthesized from BGHW through chemical activation using $ZnCl_2$. The biomass was impregnated at a 1:3 (w/v) ratio with $ZnCl_2$ solution and blended at room temperature for 12 h. The impregnated material was oven-dried at 105 °C and carbonized in a muffle furnace at 600 °C for 1 h under continuous nitrogen flow (99.99%, 200 mL/min) to ensure an inert thermal environment. The resulting carbonized product was thoroughly rinsed with deionized water until achieves a neutral pH and is dehydrated at 80 °C for 24 h.

Magnetic functionalization was achieved by dissolving iron (III) nitrate nonahydrate and $C_6H_8O_7$ in deionized water, followed by their addition to the BG-AC under stirring. The mixture was subjected to ultrasonication for 30 min to enhance dispersion and interfacial contact. The pH was adjusted to 10 using NaOH (1 M), and the suspension was refluxed at 80 °C for 2 h to promote in situ co-precipitation of Fe_3O_4 nanoparticles (Fe_3O_4@NPs). The final Fe_3O_4-functionalized carbon (BG-AC@NPs) was magnetically separated, washed with C_2H_6O and deionized water, and dried at 80 °C.

All synthesis steps were conducted under controlled laboratory conditions to ensure consistency and repeatability. Key process parameters (temperature, pH, and mass yield) were monitored using calibrated instrumentation (analytical balance=±0.1 mg; pH meter=±0.01 pH units). These procedures support the reproducible fabrication of materials with defined thermal and surface properties, suitable for subsequent adsorption and performance evaluation under measured conditions.

2.3 Physico-chemical and thermal characterization

The obtained composite material (BG-AC@NPs) was prepared via a wet-chemical route involving solution-based impregnation of Fe_3O_4@NPs onto BG-AC. The coating of NPs enhances their thermal stability and introduces surface functional groups that contribute significantly to the adsorption efficiency.

To initiate synthesis, 3 g of iron (III) nitrate nonahydrate ($Fe(NO_3)_3$ $9H_2O$) were diluted in a 50 mL solvent mixture consisting of 40% C_2H_6O and 60% distilled water. The solution was homogenized using a magnetic stirrer for 20 min. $C_6H_8O_7$ was then added while maintaining a mass ratio of 0.25 ($C_6H_8O_7$ to $Fe(NO_3)_3$ $9H_2O$). The pH of the mixture was adjusted to 5 using 0.1 M NaCl solution.

The reaction mixture was stirred under reflux conditions at 70 °C using a temperature-controlled magnetic hotplate until gelation was observed. At that point, 15 g of BG-AC were gradually introduced to the system under continuous agitation. The resulting suspension was stirred at room temperature for 1 h to ensure the uniform distribution of NPs.

The final mixture was dried at 80 °C for 48 h, followed by calcination at 400 °C for 1 h with a controlled heating rate of 5 °C/min. The obtained composite was thoroughly washed with distilled water and dried again in an oven at 105 °C for 48 h.

All thermal and pH-controlled steps were performed using calibrated laboratory instruments to ensure reproducibility and control of synthesis conditions, which were in line with best practices for the fabrication of adsorbent materials with defined structural and thermal properties.

2.3.1 Metrological considerations and measurement uncertainty

All experimental measurements were conducted using calibrated instruments, and the uncertainty associated with each measurement was evaluated according to ISO/IEC Guide 98−3 (GUM). The BET surface area was measured with an uncertainty of ±2.5%, while the pore volume and diameter were determined with a relative uncertainty of ±3%. The vibrating sample magnetometer (VSM) was performed with a resolution of 0.01 emu/g and a repeatability of ±0.5%. FTIR and XRD spectra were acquired under controlled environmental conditions, and spectral resolution was maintained at 4 cm^{-1}. All temperature-dependent experiments were conducted in thermostatic baths with a stability of ±0.1 °C. These metrological controls ensure the traceability and reproducibility of the results, in line with mechanical and thermal measurement science principles.

2.4 Characterization of BG-AC and BG-AC@NPs

The thermal stability of BG-AC and BG-AC@NPs was evaluated using a Shimadzu DTG-60 H thermal analyzer coupled with differential scanning calorimetry. The adsorbents' surface functional groups (SFGs) were analyzed through FTIR with a PerkinElmer Spectrum100 FTIR spectrophotometer, and the spectra were saved in the wavelength region of 400–4000 cm^{-1}. The crystallinity, amorphous nature, and the various polymorphs of the bulk oxides were evaluated by Bruker powder X-ray diffraction with Cu Kα radiation. The surface area, pore volume, and pore size distribution of the adsorbents were measured by a Multi-Gas Pore Capacitance Balance Sense (TRASCAN LAB 60, Digisonic) using N_2 at 77 K and calculated with the BET (Brunauer-Emmett-Teller), single-point BJH (Barrett-Joyner-Halenda) theory. Morphology and chemical compounds of the adsorbents were studied using a QuantaTM 250 FEG scanning electron microscope (SEM) in combination with energy dispersive X-ray spectroscopy (EDX). Magnetic properties were investigated for BG-AC@NPs via VSM at a magnetic field of 10 ± KI (KOe) and a range of saturation magnetization ± 8 emu/g saturation magnetization at room temperature. These techniques provide quantitative insights into the adsorbent's surface area, pore morphology, thermal stability, and magnetic response, which are crucial for assessing performance under varying environmental conditions.

2.5 Batch adsorption studies

The generation of ACE gas follows the procedure described for the solid-gas transportation phase in Fig. 1. In this experiment, vapor ACE, a solid form of ACE, serves as the ACE gas source due to its ease of decomposition, which releases ACE upon heating. Dry air, supplied by an air compressor, flows through a column containing ACE, promoting its decomposition and the release of ACE gas. The experimental conditions are maintained at 25, 30, 35, and 40 °C in a temperature-operated water bath, with an airflow rate of 8 mL min^{-1}. Fast equilibrium is achieved at 40 °C to analyze the ACE gas. Adsorption of ACE in batch mode was performed with a mass of 10, 20, 30, 40, 50, and 60 mg of BG-AC and BG-AC@NPs, respectively. The independent parameter range was 100, 200, 300, 400, 500 mg/m^3 for the initial ACE concentration, and 300 min for the contact time. The quartz fibre filters were pre-baked for 48 h at 400 °C before use. The pre-baking was described in detail by Lv et al. [37] and Isinkaralar et al. [38]. GC-MS was used to determine the ACE composition in the air extracted in the supercritical section using a PerkinElmer Clarus 680 GC/

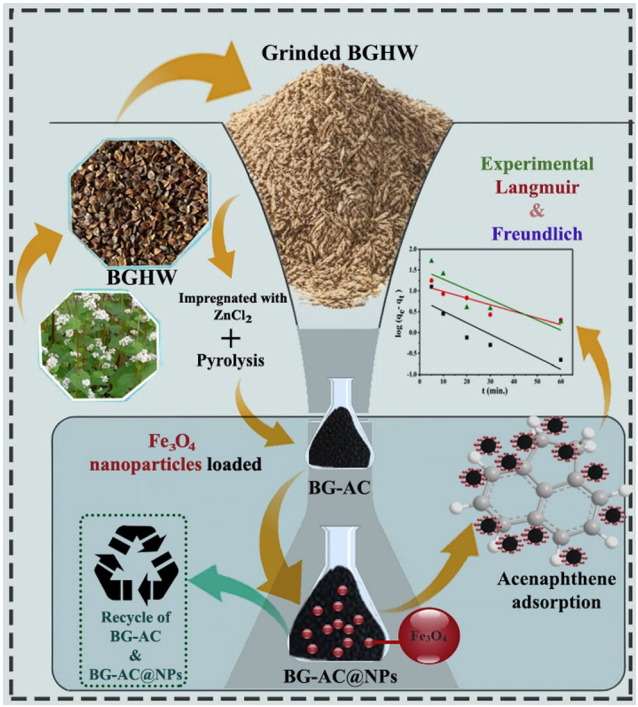

Fig. 1 Schematic diagram of ACE adsorption onto BG-AC and BG-AC@NPs

SQ8 S MS device with a 30 m x 0.25 mm x 0.25 mm film thickness Elite-5MS capillary column.

$$q_{(mg/g)} = \left(\frac{F\ x\ C_0\ x\ 10^{-9}}{W}\right)\left[\left(\frac{C_i}{C_0}\ x\ t_s\right) - \left(\int_0^{t_s}\frac{C_i}{C_0}\ d_t\right)\right] \quad (1)$$

Here t_s is the real-time outlet concentration changing with adsorption time when C_0 hits 95% equilibrium concentration of feed (mg/m^3), W (g) is the weight of adsorbent, C_i (mg/m^3) is the outlet gas concentration, and w (g) is the adsorbent mass.

2.6 Measurement models and data analysis

Several kinetic models based on various predictions were employed to examine the ACE adsorption mechanism onto the surface of BG-AC and BG-AC@NPs. In order to adequately investigate the intermolecular interactions and how these interactions are experienced by molecules on the interfaces of different adsorbents, two-parameter isotherms have been studied:

The Langmuir isotherm, a two-parameter model, is one of the most elementary and commonly utilized isotherms in describing adsorption processes [39]. Its mathematical formula is provided by Eq. (2):

$$q_e\ :\ \frac{q_m\ x\ K_L\ x\ C_e}{1\ +K_L\ C_e} \quad (2)$$

The Freundlich isotherm is commonly used to analyze multilayer adsorptions on heterogeneous surfaces [40]. Its mathematical representation is provided by Eq. (3):

$$q_e\ :K\ x\ C_e^{1/n} \quad (3)$$

The parameters of interest are the amount of ACE adsorbed at equilibrium (mg/g), as well as the content of ACE in the mixture at equilibrium (mg/L), the monolayer capacity of the adsorbent (qmax) (mg/g), and the Langmuir constant K_L (L/mg), which depends on the adsorption energy.

The Lagergren model, the so-called first-order kinetic model (PFO), assumes that the amount adsorbed varies exponentially with time [41, 42]. Equation (4) is as follows:

$$qt\ =\ qe\ (1-e^{-k1_t}) \quad (4)$$

The pseudo-second-order kinetic model (PSO) suggests that chemisorption is the primary mechanism throughout the adsorption process [43]. Following this proposed mechanism, the adsorption quantity is represented as a function of time as detailed in Eq. (5).

$$qt\ =\ \frac{qe^2K_2t}{1+qeK_2t} \quad (5)$$

where qt (mg/g) represents the amount of ACE adsorbed on BG-AC and BG-AC@NPs at time t (min). K_1 (min^{-1}) and K_2 (g mg/min) are the PFO and PSO rate constants, respectively.

The thermodynamic investigation was conducted within the 25 to 40 °C temperature range. The three thermodynamic variables were assessed. The thermodynamic parameters were determined using the equations, and the corresponding parameters, including the Gibbs free energy change ($\Delta G°$), entropy change ($\Delta S°$), and enthalpy change ($\Delta H°$) for the adsorption of ACE onto BG-AC and BG-AC@NPs, were calculated using the following Eqs. (6) and (7):

$$\Delta\ G°\ =\ \Delta\ H°\ -T\Delta\ S° \quad (6)$$

$$\mathrm{In}\ (Kc) =\ \Delta\ S°\ R - \Delta\ H°\ R\ \left(T^{-1}\right) \quad (7)$$

The equilibrium constant is obtained from graphing ln(qe/Ce) versus qe and extrapolating to zero qe. T represents the absolute temperature, and R is the universal gas constant (8.314 J K^{-1} mol^{-1}). $\Delta G°$ denotes the Gibbs free energy change in kJ·mol^{-1}, while $\Delta S°$ indicates the entropy change in kJ·mol^{-1}·K^{-1}, which is derived from the intercept of the

plot. Additionally, $\Delta H°$ signifies the enthalpy change in kJ·mol⁻¹, obtained from the slope of the plot [44]. These thermodynamic parameters are widely used to optimise and estimate the viability and spontaneity of reactions or mechanism [45].

2.7 Regeneration of BG-AC and BG-AC@NPs

The ability to regenerate and reuse adsorbents is key to their commercial feasibility, so this study focused on regenerating ACE adsorption with an initial concentration of 50 mg/m³ under optimal conditions for five consecutive adsorption-desorption cycles. The adsorbate was separated magnetically, dried in an oven at 100 °C for 30 min, and the remaining solution's residual ACE concentrations were analysed. Desorption was carried out using 0.1 g of BG-AC and BG-AC@NPs loaded with ACE molecules in 10 ml of HCl, NaOH (0.1 M), and NaCl solutions, with each solution undergoing four cycles towards the goal of regenerating and reusing the adsorbent. These desorption solutions were chosen to prevent damage or physical changes to the adsorbent structure [46], and each desorption sample was stirred at 200 rpm and 25 °C for three hours. Desorption performance was assessed by comparing the weight of desorbed ACE with the weight of ACE adhered, and the results are presented as a percentage.

3 Results and discussion

3.1 Structural, thermal, and magnetic properties

BGHW was used to convert waste biomass to generate BG-AC and BG-AC@NPs. The BGHW consists of cellulose (45.6–51.7%), hemicellulose (14.4–16.5%), lignin (28.7–31.6%), and other components (3.1–6.3%) [47]. Nitrogen physisorption isotherms were utilized to investigate the surface area and pore volume of the synthesized BG-AC and BG-AC@NPs at a constant liquid nitrogen temperature (77 K) in Fig. 2(a). The physisorption isotherms display characteristics of both type-IV behaviors with H4 hysteresis loops, implying the existence of porous and mesoporous structures within the BG-AC and BG-AC@NPs, based on the International Union of Pure and Applied Chemistry (IUPAC). The low-pressure micropore filling and the capillary condensation stages at relative pressures of 0.4 or higher revealed the analogous micro-mesoporous structures of the BG-AC and BG-AC@NPs. The surface areas (SBET) and pore volume of the BG-AC and BG-AC@NPs have been compiled in Table 1. The SBET determined from Brunauer-Emmett-Teller (BET) plots is 158.7 and 438.6 m^2/g for the BG-AC and BG-AC@NPs, respectively (Fig. 2). The pore

Fig. 2 **a** N_2 adsorption-desorption isotherm and pore size distributions; **b** magnetization curves; **c** XRD patterns; **d** FTIR spectra; SEM images of **e** BG-AC and **f** BG-AC@NPs

size distributions of the BG-AC and BG-AC@NPs were analyzed using density functional theory. The BG-AC exhibits a broad range of pore sizes (1.12 nm), from micropores (<2 nm) to mesopores (2–50 nm), whereas the BG-AC@NPs contain mesopores. The total pore volume of the BG-AC and BG-AC@NPs is 0.221 and 0.483 cm^3/g. Interestingly, the BG-AC@NPs exhibit a high DFT pore volume for pores ranging from 2 nm to 50 nm, suggesting that their structure primarily comprises mesopores (3.60 nm), which are more favorable for adsorption applications. Moreover, the disappearance of a plateau at larger P/P_0 values in the sorption isotherm further suggests the presence of macropores (>50 nm) within the samples. The broad pore size distribution, which ranges from mesopores to macropores, may result from the interlaced rectangular shape typical of BG-AC@NPs. The results demonstrate that incorporating Fe_3O_4 NPs into the AC enhanced the surface area of the adsorbent. The results acquired from the pore size distribution and adsorption isotherms align well with the XRD data and SEM image analysis.

Figure 2(b) shows that the VSM analysis proves the presence of pure Fe_3O_4 with the magnetic properties of the BG-AC@NPs. The magnetic field's ability to readily and adequately capture the magnetic media carrier at high intensity is a crucial element of this experiment [48, 49]. The magnetic saturation value of the adsorbent reaches up to 12.24 emu/g at room temperature (25 °C), and no hysteresis loops can be found in them. The results according to Fig. 2(d) suggest that BG-AC@NPs can be easily separated from the gaseous environment by a magnetic field. Li et al. [50] prepared the magnetic properties of three materials whose saturation magnetization values were highest for FeMSC (42 emu/g), followed by CoMSC (32 emu/g) and FeMAC (12 emu/g), indicating their capacity for magnetic separation from water under an external field. Remanent magnetization, a measure of retained magnetism after field removal, was highest for CoMSC (9.22 emu/g), followed by FeMSC (4.39 emu/g) and FeMAC (2.89 emu/g).

Figure 2(c) shows XRD patterns of BG-AC and BG-AC@NPs in 2θ range from 20 to 80°. The face-centered cubic structure was confirmed from the XRD patterns for the BG-AC and BG-AC@NPs in the 2θ range of 10–70°, which show a narrow diffraction peak at 2θ = 22.3° and 34.9°. The characteristic peaks of BG-AC@NPs were associated with the crystalline structure of the Fe_3O_4@NPs, which exhibited a spinel configuration. The X-ray diffraction analysis demonstrated that the Fe_3O_4@NPs were successfully synthesized and coated onto the BG-AC substrate. Furthermore,

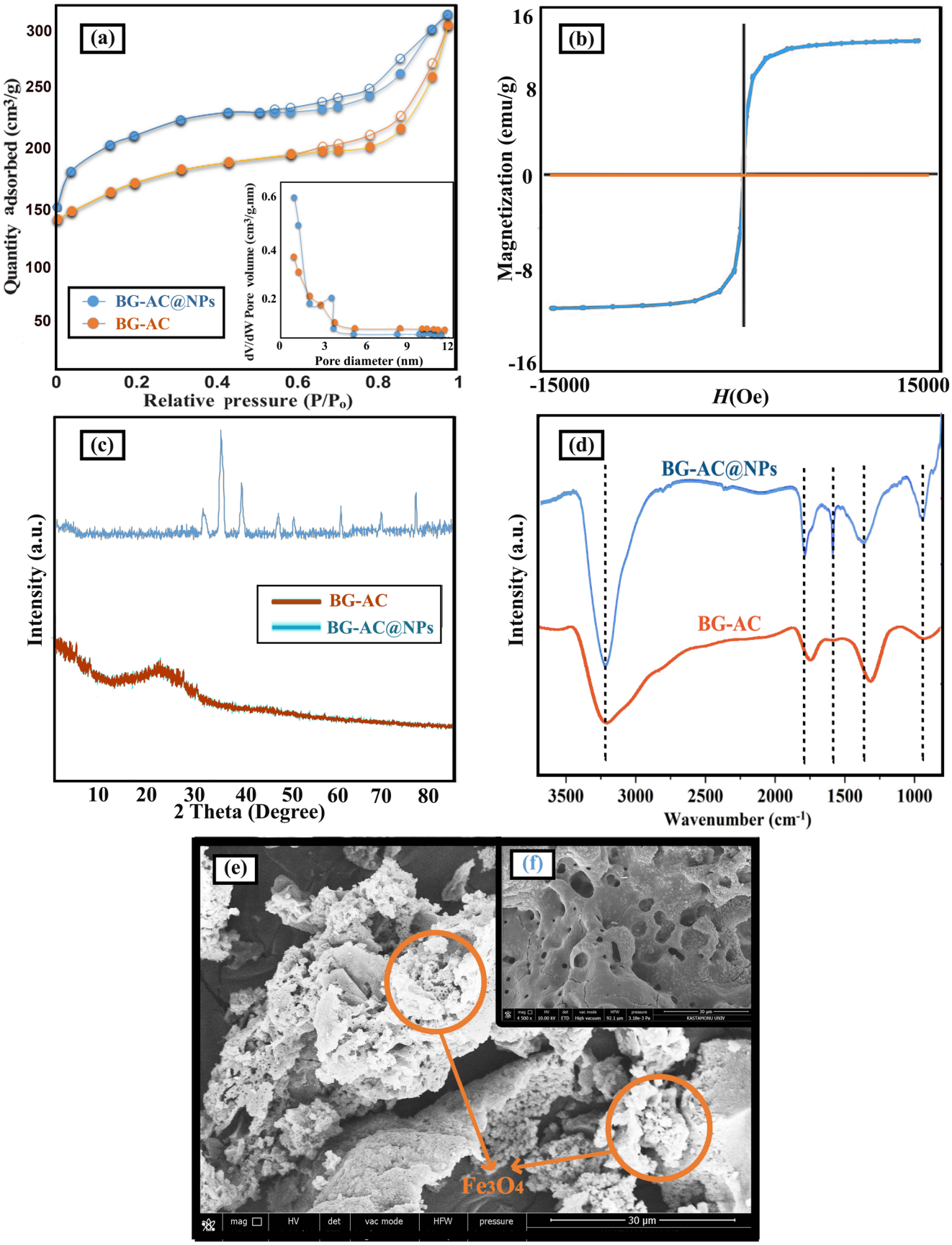
(a)
Quantity adsorbed (cm³/g)
Relative pressure (P/Po)
BG-AC@NPs
BG-AC
dV/dW Pore volume (cm³/g.nm)
Pore diameter (nm)
(b)
Magnetization (emu/g)
H(Oe)
(c)
Intensity (a.u.)
2 Theta (Degree)
BG-AC
BG-AC@NPs
(d)
Intensity (a.u.)
Wavenumber (cm-1)
BG-AC@NPs
BG-AC
(e)
(f)
Fe3O4
mag
HV
det
vac mode
HFW
pressure
30 µm

Table 1 The textural properties of BG-AC and BG-AC@NPs

Material	SBET (m^2/g)	Smicro (m^2/g)	Smeso (m^2/g)	Vtotal (cm^3/g)	Vmicro (cm^3/g)	Vmeso (cm^3/g)	Dp (nm)
BG-AC	158.7	122.9	35.8	0.221	0.128	0.093	1.12
BG-AC@NPs	438.6	304.7	133.9	0.483	0.318	0.165	3.60

SBET Specific surface area, *Smicro* Micropore specific surface area, *Smeso* Mesopore specific surface area, *Vtotal* Total pore volume, *Vmicro* Micropore volume, *Vmeso* Mesopore volume

the synthesis of BG-AC@NPs did not induce structural changes in the Fe_3O_4@NPs or the BG-AC material.

Furthermore, FTIR spectral measurements were used to determine the structural functionality of the as-synthesized samples. Figure 2(d) displays the FTIR spectrum of the as-prepared bare BG-AC and BG-AC@NPs; the broad signal at 3383 and 3321 cm^{-1} corresponds to O-H and N-H stretching vibrations, while the signal at 1748 and 1630 cm^{-1} is attributed to the C=O stretching mode. The peaks observed at 870 and 825 cm^{-1} correspond to vibrations of the FeO bond for FeO(OH), and the strong peak at 589 cm^{-1} can be assigned to the O-C-O and Fe-O bond, respectively. Specifically, the frequency associated with symmetric OH, C=C, C–H, and C–O stretching on the surface of BG-AC@NPs. The results obtained from the FTIR spectra and XRD patterns support the formation of BG-AC and BG-AC@NPs. The Fe_3O_4@MNPs@AC was characterized using field emission scanning electron microscopy, transmission electron microscopy, particle-size distribution, X-ray diffraction, and Fourier transform infrared spectroscopy [51].

SEM characterization of the pure BG-AC and BG-AC@NPs demonstrated a significant effect of Fe-impregnation on the morphological features in Fig. 2(e). A thin Fe_3O_4 layer was visible on the surface of the BG-AC@NPs due to successful Fe impregnation, which could improve the adsorption. SEM images of the as-prepared BG-AC and BG-AC@NPs reveal tightly packed interlaced structures without visible pores, indicating a dense morphology. In contrast, the SEM image confirms the presence of square-shaped structures typical of a nanocomposite; however, the compact nature suggests limited surface area accessibility. This dense structure may hinder efficiency in adsorptive applications, potentially limiting usefulness in gas/vapor treatment scenarios. SEM images of the BG-AC display a distinctly different morphology characterized by interlaced rectangular shapes with visible pores. These openings suggest a porous structure, enhancing the surface area and accessibility of the material. This porous structure offers significant benefits for adsorptive applications, enabling the removal of contaminants like ACE from the gas phase. The SEM image further confirms these findings, revealing high aspect ratio rectangular geometries indicative of a well-connected network of pores. This structure provides ample active sites for adsorption, making the BG-AC@NPs a promising candidate for wastewater remediation efforts. However, the BG-AC lacks visible pores, potentially limiting its surface area and accessibility for adsorption purposes. Therefore, these BG-AC structures may not be as effective in adsorptive removal applications as the more porous BG-AC@NPs. Similarly, Park et al. [52] study examines an Fe_3O_4-anchored AC composite as a supercapacitor electrode. The researchers found that the sample using 50 mL of an aqueous Fe3O4 dispersion in 2 g of AC had improved surface morphology, comparable surface area and porosity, and excellent electrochemical performance. The AC-50Fe composite demonstrated a maximum capacitance of 131 F/g and cyclic stability of 105% after 10,000 cycles, significantly higher than bare AC. The study concludes that the optimal Fe3O4 content can enhance supercapacitor performance by providing pseudocapacitance in addition to the double-layer capacitance of AC.

3.2 Adsorption capacity under controlled conditions

The impact of BG-AC and BG-AC@NPs on the elimination efficiency and adsorption capacity was studied by varying the ACE content. The adsorption tests were carried out by maintaining the concentration, adsorbent dose, time, and heating at 100 to 500 mg/m^3, 10 to 60 mg, 300 min, and 25 to 40 °C, respectively (Fig. 3). The elimination proficiency of gas-phase ACE at 25, 30, 35, and 40 °C and 500 mg/m^3 was augmented from 32.2 to 90.4% as BG-AC and BG-AC@NPs doses rose from 10 mg to 60 mg in Fig. 3a. However, there was no substantial improvement in elimination efficiency when the BG-AC and BG-AC@NPs doses exceeded 40 mg, indicating that the dosage value of 40 mg was the optimal value yielding 98% removal efficiency. The enhanced removal effectiveness at higher dosages is attributed to the abundant active sites that promote the adsorption of ACE. At the same time, the temperature ranges of 25 to 40 °C had a significant impact on the adsorption capacity of the BG-AC and BG-AC@NPs. The adsorption capacity dramatically diminished when we increased the dosage from 20 to 60 mg because the available active sites on BG-AC and BG-AC@NPs for the ACE molecules were absent. Elevated temperatures led to increased molecular vibrations, which may have enhanced the mobility of ACE, allowing it to gain adequate energy to bind to the active sites on the surfaces of BG-AC and BG-AC@NPs. In this direction, the

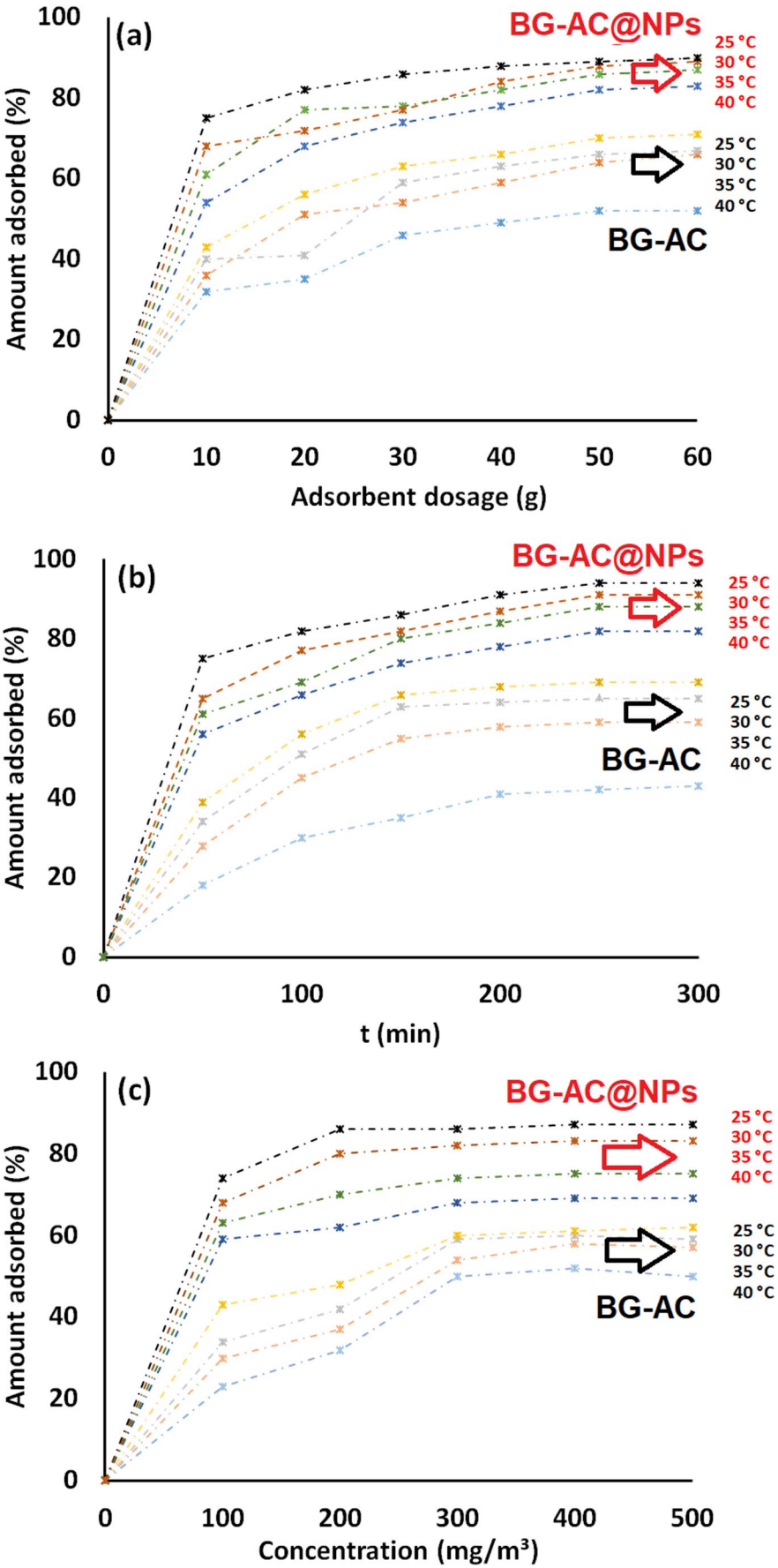

Fig. 3 Effect of (**a**) adsorbent dosage, (**b**) temperature, and (**c**) initial concentration on the adsorption of BG-AC and BG-AC@NPs

lowest value of the amount adsorbed was obtained at 32% at 25 °C, while the highest value of the amount adsorbed was increased to 90% at 40 °C. The BG-AC@NPs composites demonstrated superior removal efficiency at 40 mg, achieving a removal percentage of 86.7%. In contrast, the bare BG-AC material exhibited lower removal efficiency at 40 mg, with a percentage of 46.5% for the 500 mg/m^3 ACE vapor. The findings reported in this study are consistent with the literature reports published before. Gheitasi et al. [53] developed a sustainable powdered AC using beer barley husk, an agricultural waste. They modified the PAC with SH and employed it as an eco-friendly adsorbent to remove mercury from contaminated water. The study entailed a two-step chemical activation with magnetic iron salt for easy separation, synthesizing a thiol-modified magnetic AC adsorbent of mPAC-SH through a straightforward and safe hydrothermal method. The synthesized mPAC-SH magnetic nanocomposite was then used to remove Hg^{+2} ions from the aqueous solution. The study revealed the highest removal rate of 99.44% under optimal conditions: pH = 6, mercury concentrations around 20 mg/L, adsorbent dose of 0.4 g/L, and contact time of 60 min.

The adsorption process was examined by varying the working concentrations of ACE (selected optimum gas concentration for 300 mg/m^3) and contact times (300 min), while maintaining the ideal dosage (at 40 mg), and temperature between 25 and 40 °C, respectively. When the contact time changed from 0 to 300 min, the adsorption capacity rose sharply before reaching a saturation level for all initial concentrations (Fig. 3b). The steep rise in adsorption capacity of up to 150 min is attributed to the extensive adsorption sites on ACE's BG-AC and BG-AC@NPs structure. Further increases in contact time beyond 150 min revealed a steady-state adsorption capacity trend, indicating that the adsorbent surface reached saturation, with negligible ACE uptake occurring thereafter. As a result, 150 min was taken as the optimal contact time for all initial concentrations shown in Fig. 3c.

Additionally, the ACE elimination performance of BG-AC and BG-AC@NPs was examined by varying the initial concentration of ACE. The removal efficiency decreased with increasing initial ACE concentration due to competition among the ACE for effective binding to the inactive active sites on the BG-AC and BG-AC@NPs surface. This led to a continuous decrease in ACE removal efficiency with an increase in initial feed concentration. For BG-AC, it was observed that a temperature of 40 °C resulted in the highest maximum removal efficiency, which was achieved at 150 min. This was due to the greater concentration of active sites available at the start of the experiment. Subsequently, the number of available sites decreased until an equilibrium state was reached around 200 min. In the BG-AC@NPs composites, gas-phase ACE removal efficiency reached 91.2% and 94.3% at 200 and 250 min, respectively. Pure BG-AC did not perform effectively at 30 °C with 59% of its capacity. The BG-AC@NPs composite demonstrated clear benefits, as it enhanced the efficiency in removing the vapor ACE. Compared to the standalone BG-AC, the BG-AC@NPs consistently exhibited higher removal efficiency percentages. Juang et al. [54] found that the adsorption capacity of methyl orange at 30 °C slightly decreased from 384 mg/g on AC powders to 324 mg/g on Fe_3O_4@AC nanocomposites and such a structure is seldom observed in other similar previous studies.

3.3 Adsorption kinetics and thermodynamic behavior

The Langmuir and Freundlich models were used to examine the adsorption behavior of ACE onto BG-AC and BG-AC@NPs. The relevant equations and descriptions were provided in the supporting information. Figure 4 depicts a linearized isotherm for all cases, with the corresponding input presented in Table 2. The R^2 values derived from the Langmuir and Freundlich graphs of BG-AC and BG-AC@NPs were found to be 0.965 and 0.988, respectively. In general, the best-fit model followed the sequence of Langmuir > Freundlich model based on the R^2 value. These values indicate that the Langmuir model best fits the experimental findings, demonstrating that the adsorption of ACE is uniform and monolayer in nature over BG-AC [55]. We obtained an adsorption capacity of up to 118.9 mg/g and 378.3 mg/g using BG-AC and BG-AC@NPs. The determined qmax value in this study is considerably greater than the values reported for BG-AC and BG-AC@NPs. This indicates that BG-AC@NPs effectively eliminate ACE from the gas stream. The BG-AC and BG-AC@NPs were utilized to differentiate chemisorption, as the Freundlich isotherms do not provide this information directly. Guo et al. [56] describe a method for creating Fe-Mg bimetallic magnetic ACs (Fe–Mg BACs) using peanut shells as a precursor to achieve high adsorption performance for malachite green dye. During the activation process under a CO_2 atmosphere, MgO NPs were formed and aggregated with Fe_3O_4, resulting in MgO/Fe_3O_4@NPs on the surface of the carbon basal plane. The material, Fe–Mg15, achieved a large MG adsorption capacity of 4031.96 mg/g at 318 K. The formation of MgO/Fe_3O_4 composite NPs is proposed to be the active sites influencing the adsorption performance. The study also found that the PFO and Freundlich models best described the adsorption process, suggesting a chemisorption mechanism. Al-Musawi et al. [57] focus on preparing magnetized AC (Fe_3O_4–HSAC) by activating hazelnut shell waste and then coating it with Fe_3O_4@NPs. The prepared

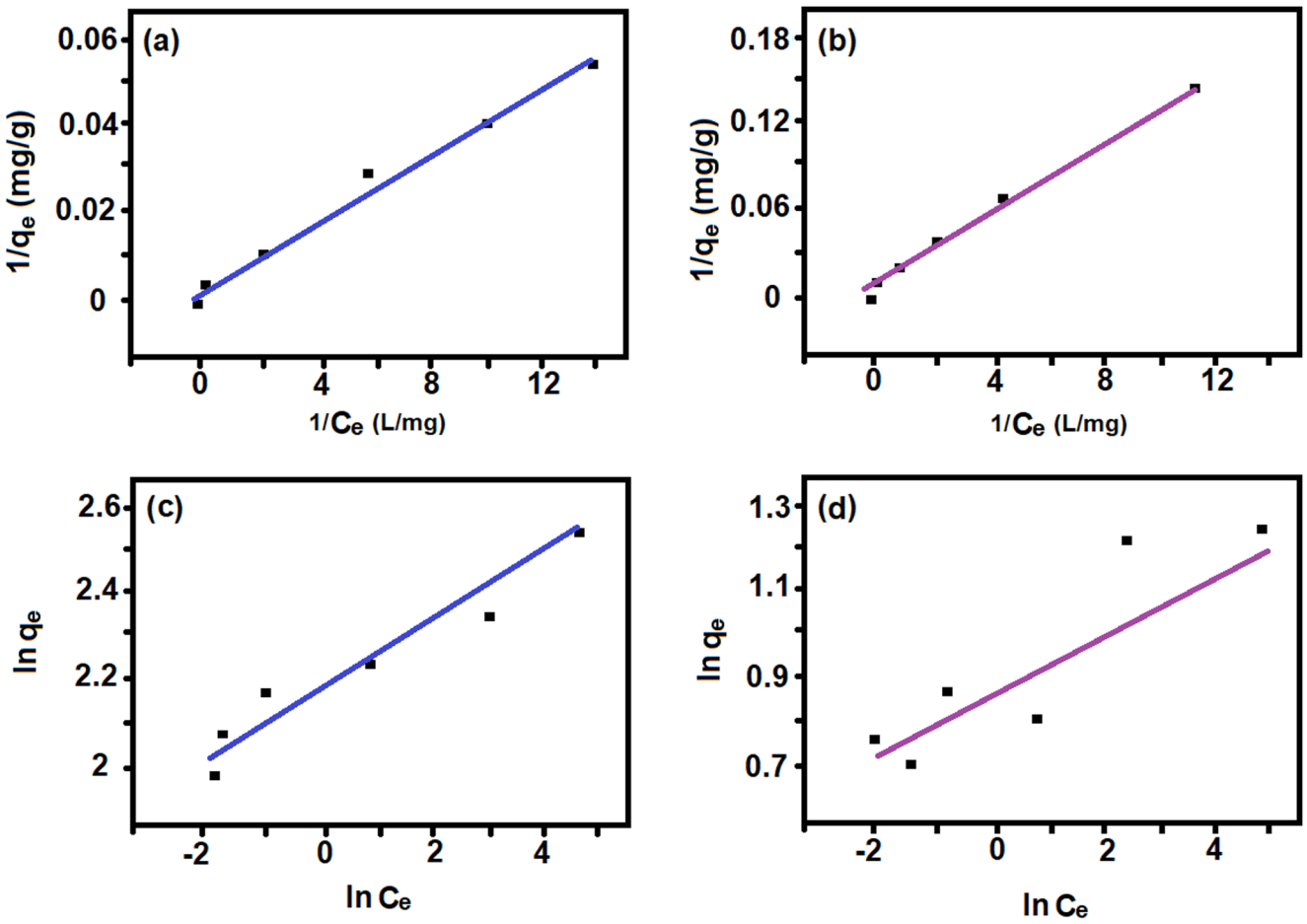

Fig. 4 Linearized isotherm models of (**a**) Langmuir type for ACE adsorption onto BG-AC, (**b**) Langmuir type for ACE adsorption onto BG-AC@NPs, (**c**) Freundlich ACE adsorption onto BG-AC, and (**d**) Freundlich ACE adsorption onto BG-AC@NPs

Table 2 Isotherm models for ACE adsorption using BG-AC and BG-AC@NPs at 25 °C

Type of isotherms	Model equation	Parameters	Corresponding values	
			BG-AC	BG-AC@NPs
Langmuir	$qe = \frac{qmaxbCe}{1+bCe}$	b (L/mg)	0.0056	1.88
		qm (mg/g)	118.9	378.3
		R^2	0.965	0.988
Freundlich	$qe = K_F C_e^{1/n}$	$1/n$	0.342	0.536
		K_F	62.18	277.3
		R^2	0.935	0.884

Fe_3O_4–HSAC was tested as an adsorbent for fluoride removal under different conditions. The study found that the Fe_3O_4–HSAC can remove 100% of fluoride under optimal conditions (adsorbent dose = 0.75 g/L; pH = 3–5; and temperature = 323 K). The maximum adsorption capacity was 146.2 mg/g at 298 K and pH 5. The study also found that the adsorption process is controlled by both intraparticle diffusion and liquid film diffusion. The physical adsorption was predominant. Mohammadifard et al. [58] compare the effectiveness of magnetic ACs made from banana peel and Salvia seed in removing basic blue 41 dye from water. The study examines the capability of the produced ACs to remove basic blue 41 dye from aqueous solutions using batch adsorption under various operating conditions such as pH, adsorbent dose, initial adsorbate concentration, and contact time. The optimal conditions for dye adsorption using BPAC@Fe_3O_4 were a pH of 9, an adsorbent dose of 0.5 g/L, a dye concentration of 50 mg/L, and an equilibrium contact time of 30 min. Similarly, the ideal dye adsorption conditions for SSAC@Fe_3O_4 were a pH of 9, an adsorbent dose of 0.75 mg/L, a dye concentration of 50 mg/L, and an equilibrium contact time of 30 min. The study also determined that the Langmuir isotherm model provided an excellent fit, with a regression coefficient of $R^2 = 0.9886$. Zadeh & Jafari [59] investigate the efficiency of a synthesized AC/alginate/Fe_3O_4 composite adsorbent for removing Pb ions from water. The composite was characterized using various methods, and the optimal adsorption parameters were determined through experiments. The study found that optimal adsorption efficiency was 97.83% under optimal conditions. The Freundlich isotherm model described the equilibrium of the process better than the Langmuir model, indicating

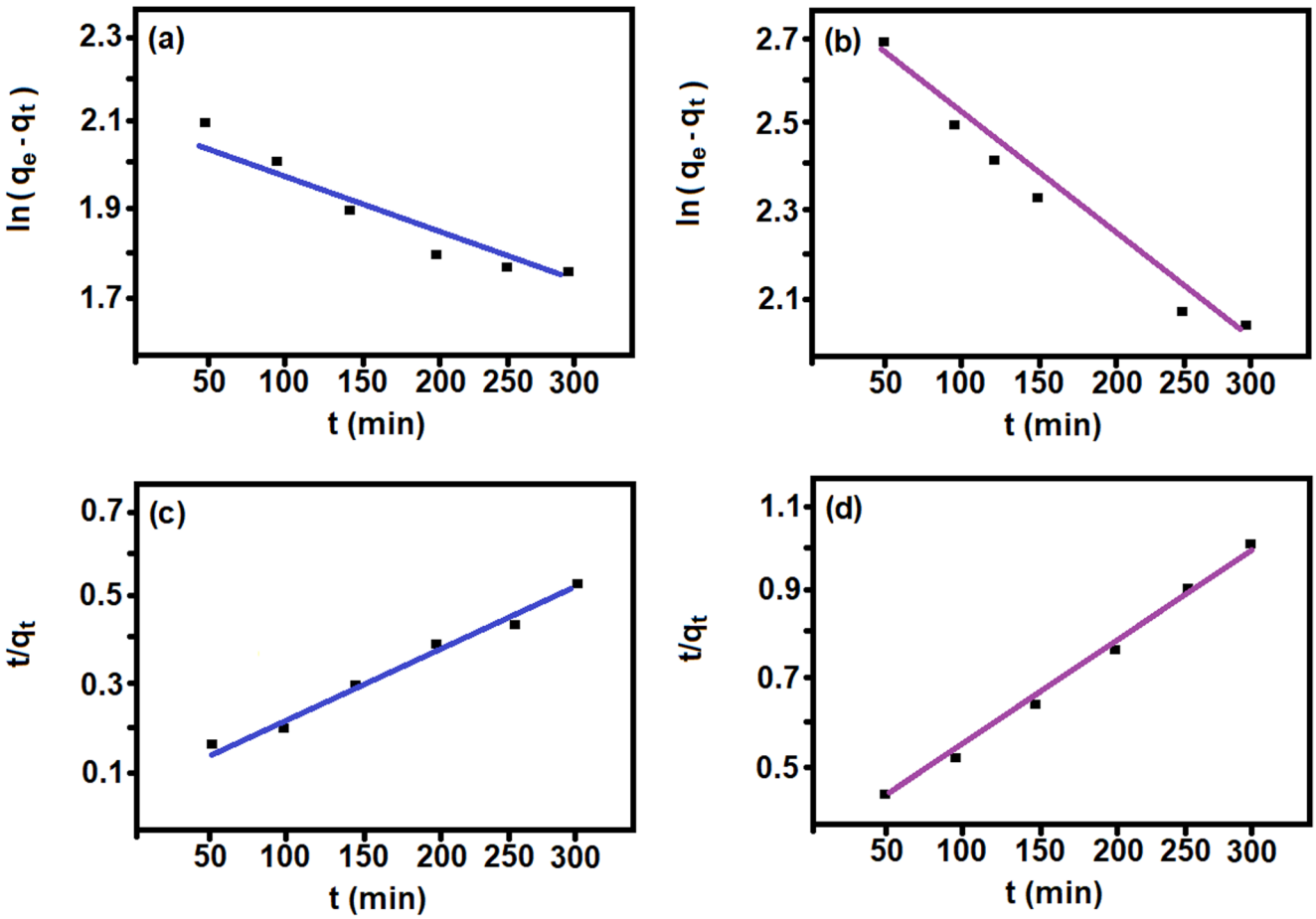

Fig. 5 Kinetic studies for ACE adsorption over the BG-AC and BG-AC@NPs (**a**) PFO for BG-AC, (**b**) PFO for BG-AC@NPs, (**c**) PSO for BG-AC, and (**d**) PSO for BG-AC@NPs

Table 3 Kinetic studies revealing ACE adsorption onto BG-AC and BG-AC@NPs

Type of kinetic model	Model equation	Parameters	Values	
			BG-AC	BG-AC@NPs
PFO	$\ln(q_e - q_t) = \ln q_e - K_1 t$	q_e (mg/g)	21.53	126.5
		K_1 (min)	0.0183	0.076
		R^2	0.823	0.984
PSO	$\frac{t}{q} = \left[\frac{1}{K_2 q_e^2} + \frac{1}{q_e}\right]$	q_{et} (mg/g)	60.98	327.6
	$(mg/g\ min)$	K_2	0.0028	0.0013
		R^2	0.993	0.941

that lead ions were adsorbed on a heterogeneous surface. The maximum adsorption capacity of the adsorbent was 37.764 mg/g, and the process followed the PSO kinetic model. The process was also endothermic.

3.3.1 Adsorption kinetics

To explore the kinetics of ACE over the BG-AC and BG-AC@NPs surface, we conducted kinetic studies under optimal conditions: a concentration of 100 mg/m^3, and a temperature of 25 °C. The findings were analyzed using the PFO and PSO kinetic equations. Figure 5 displays the linear curve fitting for each model. The rate constant, correlation coefficient (R^2), and adsorption capacity for each kinetic model are presented in Table 3. The R^2 value for the PFO of BG-AC and BG-AC@NPs was 0.823 and 0984, indicating a relatively poor fit with the PFO equation. However, the experimental data fitted to the PSO kinetic model shows the highest R^2 value, close to unity. This indicates that the removal rate of ACE likely occurred through a chemisorption route, possibly due to the attraction between ACE and the reactive groups on the BG-AC and BG-AC@NPs. The removal rate of ACE was notably rapid in the early stages of adsorption, gradually stabilizing until it reached equilibrium between 200 and 250 min. The qe value obtained from the PSO model (60.98 mg/g and 327.6 mg/g) closely matched the experimental qe value (61.5 mg/g and 335.6 mg/g), further confirming the suitability of the PSO model. These findings are consistent with previous research on removing ACE using other adsorbents [60, 61]. The PFO and PSO models were employed to investigate the rate-limiting step further and determine the kinetic nature of adsorption on the

BG-AC and BG-AC@NPs surfaces. The corresponding R^2 values obtained from these models were lower than the R^2 value obtained from the PSO, implying that the PSO most accurately describes the adsorption kinetics of ACE on the BG-AC and BG-AC@NPs adsorbent. Do et al. [62] report that the methyl orange adsorption process on the composites conformed to a PSO kinetic model. The findings indicated that the MO adsorption process on the composites followed a PSO kinetic model, and the adsorption isotherm data could be simulated using the Freundlich and Langmuir models. Lincold et al. [63] focus on enhancing the adsorption of malachite green dye using AC from black fruit kernels modified with Fe_3O_4 NPs. The composite material was characterized using various techniques, and the effects of different factors such as contact time, pH, concentration, and temperature were evaluated. Adding NPs decreased the surface area but increased the maximum adsorption capacity (600–700 mg/g). Hill's isotherm best describes the adsorption process and follows a PSO model. The adsorption enthalpy suggests a transition from exothermic physisorption to endothermic chemisorption due to the introduction of functional surfaces with increased adsorption capacity by the Fe_3O_4@NPs.

Table 4 summarizes the sorption of PAHs onto various sorbents based on NPs derived from certain types of AC. Several materials display relatively low sorption capacities in aqueous solutions or gaseous environments. However, the sorptive capabilities of carbonaceous materials are substantially improved after being loaded with Fe_3O_4 NPs, as demonstrated in studies using different types of sorption reactors. Liu et al. [64] focus on using a composite material of Fe_3O_4@NPs and AC (Fe_3O_4/AC) to remove Acid red 73 from wastewater. The Fe_3O_4/AC composite has enhanced surface area and magnetic properties, enabling efficient dye adsorption and easy separation from the water [65]. The study explores the adsorption behavior through experiments and discusses the physical and chemical mechanisms involved. The authors also assessed the regeneration and recyclability of the Fe_3O_4@NPs@AC. Kakavandi et al. [66] explore the use of a magnetic composite material (Fe_3O_4@C) made of AC and superparamagnetic Fe_3O_4@NPs to remove lead ions (Pb^{+2}) from water. The composite combines the adsorption properties of AC with the ease of magnetic separation, offering a potential solution to difficulties in filtration and centrifugation. The study examines the composite's characteristics, various factors' effects on lead adsorption, and the material's regeneration potential. The results suggest that Fe_3O_4@AC is a promising material for removing Pb^{+2} from aqueous solutions. The sorption capacity of the enhanced materials with Fe_3O_4@NPs was even higher than that of certain types of non-modified AC.

3.3.2 Model comparison and error analysis

This section compares the kinetic models (PFO and PSO) and isotherm models (Langmuir and Freundlich) used in our study. The performance of each model was evaluated using the coefficient of determination (R^2), which the PFO model showed a relatively lower R^2 value (0.823 for BG-AC and 0.984 for BG-AC@NPs) compared to the PSO model (0.993 for BG-AC and 0.941 for BG-AC@NPs), indicating a better fit to the experimental data.

For the isotherm models, the Langmuir model exhibited a higher R^2 value (0.965 for BG-AC and 0.988 for BG-AC@NPs) compared to the Freundlich model (0.935 for BG-AC and 0.884 for BG-AC@NPs), indicating a better fit to the equilibrium data. The R^2 values also supported this observation, with the Langmuir model showing a higher R^2 for BG-AC@NPs. The sensitivity analysis revealed that the adsorption capacity (qmax) in the Langmuir model was more sensitive to changes in temperature. At the same time, the Freundlich constant (K_F) was more affected by

Table 4 Based on literature data, the PAHs sorption capacity of the Fe_3O_4 NPs functionalized AC

Sorbent	For what purpose was it produced?	Initial concentration	Sorption capacity (mg/g)	Sorption time (min)	Efficiency of adsorption process (%)	References
ACL/Fe_3O_4	Cationic dye of crystal violet	10–80 mg/L	35.3 mg/g	5–140	98.3	Foroutan et al. [67]
Fe_3O_4@AC	Methylene blue and brilliant green dyes	30–100 mg/L	138-166.6 mg/g	0.20–120	73.8–100	Joshi et al. [68]
BG-AC@NPs	ACE	100–500 mg/m^3	378.3 mg/g	300	94.3	In this study
AC/Fe_3O_4	Formaldehyde	5–50 mg/L	24.21 mg/g	5-150	95.67	Khaleghi et al. [69]
MAC	4-chlorophenol	5-100 mg/L	128.2 mg/g	0-300	95	Duan et al. [70]
(1.5%)Fe_3O_4/GAC	methane	10.3 mmol/L	388.1 mL CH4/g COD	4320	90.4–97.1	Orrantia et al. [71]
MAC	2,4-dichlorophenoxyacetic (2,4-D) acid	50–300 ppm	79.05 mg/g	3-300	91.92	Herrera-García et al. [72]
MPAC	PAHs	2.5 ppm	-	2880	87.2–99.3	Mirzaee and Sartaj [73]
SABC	PAHs	3114 µg/kg	-	2880	≥80%	Carlini et al. [74]

variations in adsorbate concentration. Similarly, the rate constant (k_1) in the PFO model was more sensitive to temperature changes, whereas the PSO model parameters were relatively stable under varying conditions.

These findings highlight the importance of selecting appropriate models based on the specific experimental conditions and the nature of the adsorbate-adsorbent interactions.

3.3.3 Adsorption thermodynamics

The impact of temperature was also examined at variable temperatures to obtain more insights into the adsorption process in Table 5. The free energy change (ΔG_0) value was evaluated using Eq. 6, while the (ΔH_0) and the (ΔS_0) values were evaluated using Eq. 7. The relationship between *ln KT* and 1/T, reveals a linear trend with ΔH_0/R and ΔS_0/R representing the slope and intercept, respectively. The values of ΔH_0 and ΔS_0 over BG-AC and BG-AC@NPs were found to be −11.983 kJ mol^{-1} and 51.354 kJ mol^{-1}; 0.032 J mol^{-1} K^{-1} and 0.024 J mol^{-1} K^{-1}, respectively, indicating that the adsorption process is endothermic. The positive $\Delta S°$ value suggests an increase in randomness at the sorbent-sorbate interface, while the magnitude of ΔH_0 indicates the presence of strong physical interactions, particularly electrostatic attractions, between the bulk and solid phases [75]. Additionally, the changes in Gibbs free energy (ΔG_0) over BG-AC and BG-AC@NPs were recorded at each temperature point, showing moderate incremental negativity: −0.196, −0.564, −0.698, and −0.447 kJ mol^{-1}; −0.823, −3.058, and −6.336 kJ mol^{-1}, indicating that the adsorption is both spontaneous and endothermic except 0.573 kJ mol^{-1} for BG-AC@NPs at 25 °C. Negative values for Gibbs' free energy indicated that the adsorption process for both adsorbents was physical. To further assess the feasibility of adsorption, we evaluated the dimensionless separation factor (R_L) using the equation provided in the supporting information. Its value ranged from 0.03 to 0.003, suggesting that the adsorption process of ACE is favorable, as these R_L values fall within the acceptable range of $0 \leq RL \leq 1$. The adsorption isotherm would be unfavorable for $R_L > 1.0$, linear for $RL = 1.0$, and irreversible for $R_L = 0$ [76]. Badi et al. [77] investigated using powder-AC modified with magnetite NPs to remove the antibiotic Ceftriaxone from water. The PAC-MNPs composite was synthesized using co-precipitation and characterized using TEM, SEM, and XRD. The study optimized the removal process using response surface methodology, examining factors like pH, initial Ceftriaxone concentration, temperature, and adsorbent dosage. The results showed that the composite effectively removes Ceftriaxone, with the adsorption process being spontaneous and exothermic. The material could also be regenerated and reused for multiple cycles with minimal loss in efficiency. The use of magnetic NPs helps with the separation of the absorbent from the water. These values indicate that the adsorption of ACE on BG-AC and BG-AC@NPs is spontaneous and feasible, likely due to the high surface area of the as-prepared adsorbent. The determined thermodynamic parameters provide valuable insights into the mechanisms that govern the adsorption of ACE on BG-AC@NPs. This understanding can help optimize conditions for various applications, including environmental remediation and catalysis.

Table 5 Thermodynamic studies of ACE adsorption over BG-AC and BG-AC@NPs

Adsorbent	T (K)	ΔG (kJ mol^{-1})	ΔH (kJ mol^{-1})	ΔS (kJ mol^{-1} K)
BG-AC	25	−0.196	−11.983	0.032
	30	−0.564		
	35	−0.698		
	40	−0.447		
BG-AC@NPs	25	0.573	51.354	0.024
	30	−0.823		
	35	−3.058		
	40	−6.336		

3.4 Reusability and regeneration efficiency

The results are presented in Fig. 6. The results show that the adsorption percentage of ACE by BG-AC@NPs and BG-AC non-significantly decreased from 94 to 43% and 82 to 18% after five cycles. This suggests the BG-AC@NPs can be recycled and reused for three successive cycles with an adsorption efficiency > 80%. The optimum conditions for PAHs removal were determined, and the results showed high suitability of the method for gas treatment due to the easy separation and good regeneration of the NPs. It can be concluded that BG-AC@NPs have good potential for regeneration and reusability. Therefore, based on simple and easy regeneration, it can be an economical and effective adsorbent for ACE removal from the gaseous environment in industrial applications. Aungthitipan et al. [78] investigated the adsorption and desorption cycle performance of hardwood-PRPW biochar composites, whose initial adsorption efficiency was 87.58%, decreasing to 68.81% by the fourth cycle. Similarly, desorption efficiency decreased from 79.15 to 43.62% over the same duration. This decline suggests a progressive degradation in the adsorbent's ion capture and release capacity. Potential causes for this reduction in efficiency include damage to the support structure, surface obstruction, incomplete desorption, or the deactivation of active binding sites on the adsorbent material. To enhance material reusability and maintain efficiency, chemical sorbent regeneration, improved handling of the sorbent,

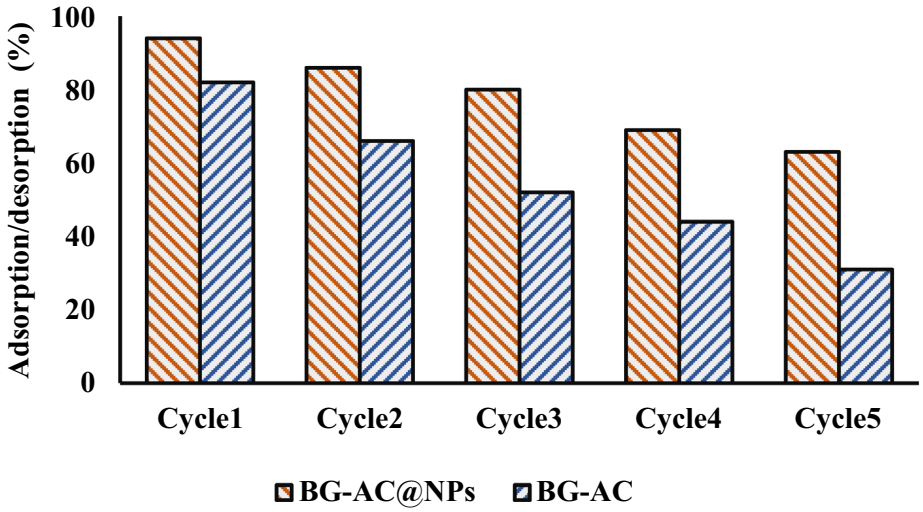

Fig. 6 Four cycles of ACE adsorption–desorption (contact time = 120 min, initial ACE concentration = 50 mg/m^3, and T = 25 °C)

or surface modifications could be considered by Tansomros et al. [79]. These strategies may sustain enhanced environmental pollutant removal efficiencies across multiple cycles.

3.5 Environmental metrology and technical standards

In this section, we discuss the relevance of our experimental results to environmental metrology and technical standards. The adsorption performance of Fe_3O_4@activated carbon for gas-phase PAH removal was evaluated by ISO and UNI standards for air quality and material characterization. The experimental setup and procedures were designed to comply with ISO 16000-6 for indoor air quality and ISO 11,357 for thermal analysis. The adsorption isotherms and kinetic models were validated against UNI EN 12,341 for particulate matter and UNI EN 14,907 for gravimetric analysis.

The BET surface area measurements followed ISO 9277, accurately determining specific surface area and porosity. The VSM magnetization measurements were performed following ISO 11,358 for thermogravimetric analysis, providing reliable data on the magnetic properties of the adsorbent.

The FTIR and XRD analyses were carried out under controlled environmental conditions, adhering to ISO 10,694 for infrared spectroscopy and ISO 13,320 for particle size analysis. These metrological controls and adherence to technical standards ensure our results' traceability, reproducibility, and comparability, contributing to the development of standardized methods for environmental monitoring and material characterization.

4 Conclusions

ACE in indoor environments, often resulting from excessive use of reactive organic and inorganic compounds, is a significant health concern, particularly for sensitive populations. This study highlights that elevated levels of gas-phase and low molecular weight PAHs are linked to adverse effects on air quality, especially in urban settings. To address this, a tailored adsorbent system based on buckeheat husk-derived activated carbon (BG-AC) and its iron-oxide-functionalized variant (BG-AC@NPs) was synthesized via $ZnCl_2$ nanoparticle impregnation. The experimental evaluation in a batch adsorption reactor demonstrated that both BG-AC and BG-AC@NPs effectively reduced the gas-phase concentration of ACE, with removal efficiencies between 20 and 40% under controlled conditions. The improved performance of BG-AC@NP is primarily attributed to its enriched surface functional groups and the presence of Fe_3O_4 layers, which enhance adsorption through multiple mechanisms. Quantitative analysis confirmed that the Langmuir isotherm and PSO kinetic model best describe the adsorption behavior, suggesting monolayer coverage and chemisorption dominance. The maximum adsorption capacity, determined through Langmuir fitting, reached 378.3 mg/g, highlighting the material's high affinity for ACE. Thermodynamic measurements showed positive enthalpy and entropy changes, indicating that the adsorption is endothermic and disorder-increasing, while the negative Gibbs free energy values confirmed its spontaneous nature under the tested conditions. These findings provide a robust experimental framework for evaluating and optimizing adsorbent performance through thermal and kinetic measurements. Future work will improve the material's efficacy by optimizing Fe content and dosing strategies to enhance its applicability in

gas-phase PAH monitoring and environmental risk mitigation systems.

Finally, the study contributes to the development and metrological evaluation of advanced adsorbent materials, integrating thermal and mechanical measurement techniques under controlled physico-chemical conditions.

Author contributions Kaan Isinkaralar, Antonio Cannuli. Conceptualization, Investigation, Methodology, Writing – original draft. Aydin Turkyilmaz: Data curation, Investigation, Writing - review & editing. Huseyin Guran Unal: Formal analysis, Writing - review & editing. Chander Prakash: Writing - review & editing. Ahmad Hosseini-Bandegharaei, Antonio Cannuli: Methodology, Validation, Writing - review & editing.

Funding This research was funded by European Union's Next Generation EU, project MUR, PNRR-M4C2, ECS_00000022—SAMOTHRACE (Sicilian Micro and Nano Technology Research and Innovation Center).

Data availability No datasets were generated or analysed during the current study.

Declarations

Ethics approval All authors have read, understood, and have complied as applicable with the statement on "Ethical responsibilities of Authors" as found in the Instructions for Authors.

Competing interests The authors declare no competing interests.

References

1. K. Szramowiat-Sala, M. Marczak-Grzesik, M. Karczewski, M. Kistler, A.K. Giebl, K. Styszko, Chemical investigation of polycyclic aromatic hydrocarbon sources in an urban area with complex air quality challenges. Sci. Rep. **15**(1), 6987 (2025). https://doi.org/10.1038/s41598-025-91018-8
2. K.H. Kim, S.A. Jahan, E. Kabir, R.J. Brown, A review of airborne polycyclic aromatic hydrocarbons (PAHs) and their human health effects. Environ. Int. **60**, 71–80 (2013). https://doi.org/10.1016/j.envint.2013.07.019
3. A.A. Jamhari, M. Sahani, M.T. Latif, K.M. Chan, H.S. Tan, M.F. Khan, N.M. Tahir, Concentration and source identification of polycyclic aromatic hydrocarbons (PAHs) in PM10 of urban, industrial and semi-urban areas in Malaysia. Atmos. Environ. **86**, 16–27 (2014). https://doi.org/10.1016/j.atmosenv.2013.12.019
4. R. Atkinson, J. Arey, Atmospheric chemistry of gas-phase polycyclic aromatic hydrocarbons: formation of atmospheric mutagens. Environ. Health Perspect. **102**(suppl 4), 117–126 (1994). https://doi.org/10.1289/ehp.94102s411
5. J. Ishtiaq, J.H. Syed, W.A. Jadoon, N. Hamid, M.J.I. Chaudhry, M. Shahnawaz, J. Nasir, S.H.H. Rizvi, P. Chakraborty, G. Zhang, Atmospheric polycyclic aromatic hydrocarbons (PAHs) at urban settings in Pakistan: spatial variations, sources and health risks. Chemosphere **274**, 129811 (2021). https://doi.org/10.1016/j.chemosphere.2021.129811
6. S. Wongcharee, V. Aravinthan, L. Erdei, W. Sanongraj, Mesoporous activated carbon prepared from macadamia nut shell waste by carbon dioxide activation: C omparative characterisation and study of methylene blue removal from aqueous solution. Asia-Pac. J. Chem. Eng. **13**(2), e2179 (2018). https://doi.org/10.1002/apj.2179
7. K.S. Ukanwa, K. Patchigolla, R. Sakrabani, E. Anthony, S. Mandavgane, A review of chemicals to produce activated carbon from agricultural waste biomass. Sustainability **11**(22), 6204 (2019). https://doi.org/10.3390/su11226204
8. H.A. Alhashimi, C.B. Aktas, Life cycle environmental and economic performance of biochar compared with activated carbon: a meta-analysis. Resour. Conserv. Recycl. **118**, 13–26 (2017). https://doi.org/10.1016/j.resconrec.2016.11.016
9. X.F. Tan, S.B. Liu, Y.G. Liu, Y.L. Gu, G.M. Zeng, X.J. Hu, X. Wang, S.H. Lu, L.H. Jiang, Biochar as potential sustainable precursors for activated carbon production: multiple applications in environmental protection and energy storage. Bioresour. Technol. **227**, 359–372 (2017). https://doi.org/10.1016/j.biortech.2016.12.083
10. M. Gayathiri, T. Pulingam, K.T. Lee, K. Sudesh, Activated carbon from biomass waste precursors: factors affecting production and adsorption mechanism. Chemosphere. **294**, 133764 (2022). https://doi.org/10.1016/j.chemosphere.2022.133764
11. K. Isinkaralar, A. Turkyilmaz, H.G. Ünal, A. Hosseini-Bandegharaei, Enhancing a novel Al2O3–Chitosan@ activated carbon nanocomposite for indoor air quality: examination of vapor-phase phenanthrene adsorption efficiency of air cleaner material. J. Mol. Struct. **1336**, 142126 (2025). https://doi.org/10.1016/j.molstruc.2025.142126
12. E.N. Coker, X. Lujan-Flores, B. Donaldson, N. Yilmaz, A. Atmanli, An assessment of the conversion of biomass and industrial waste products to activated carbon. Energies. **16**(4), 1606 (2023). https://doi.org/10.3390/en16041606
13. G.L. Sullivan, R.M. Prigmore, P. Knight, A.R. Godfrey, Activated carbon biochar from municipal waste as a sorptive agent for the removal of polyaromatic hydrocarbons (PAHs), phenols and petroleum based compounds in contaminated liquids. J. Environ. Manage. **251**, 109551 (2019). https://doi.org/10.1016/j.jenvman.2019.109551
14. H. Xu, M.X. Zhan, P.T. Cai, L.J. Ji, T. Chen, X.D. Li, Adsorption characteristics of polycyclic aromatic hydrocarbons by biomass-activated carbon. Flue Gas Energy Fuels. **33**(11), 11477–11485 (2019). https://doi.org/10.1021/acs.energyfuels.9b02723
15. K. Isinkaralar, Adsorption of gaseous naphthalene on carbonaceous sorbent: perspective of affecting factors. Biomass Convers. Biorefin. **15**, 2579–2586 (2025). https://doi.org/10.1007/s13399-023-04755-z
16. M. Zeng, Z. Liao, L. Wang, Atmospheric oxidation of gaseous anthracene and phenanthrene initiated by OH radicals. Atmos. Environ. **234**, 117587 (2020). https://doi.org/10.1016/j.atmosenv.2020.117587
17. L. Wang, L. Wang, Atmospheric oxidation mechanism of acenaphthene initiated by OH radicals. Atmos. Environ. **243**, 117870 (2020). https://doi.org/10.1016/j.atmosenv.2020.117870
18. H. Vistnes, N.A. Sossalla, A. Røsvik, S.V. Gonzalez, J. Zhang, T. Meyn, A.G. Asimakopoulos, The determination of polycyclic aromatic hydrocarbons (PAHs) with HPLC-DAD-FLD and GC-MS techniques in the dissolved and particulate phase of road-tunnel wash water: a case study for cross-array comparisons and applications. Toxics **10**(7), 399 (2022). https://doi.org/10.3390/toxics10070399
19. A.A. Akinpelu, M.E. Ali, M.R. Johan, R. Saidur, M.A. Qurban, T.A. Saleh, Polycyclic aromatic hydrocarbons extraction and removal from wastewater by carbon nanotubes: a review of the current technologies, challenges and prospects. Process Saf. Environ. Prot. **122**, 68–82 (2019). https://doi.org/10.1016/j.psep.2018.11.006

20. Z. Li, Y. Liu, X. Yang, Y. Xing, Q. Yang, R.T. Yang, Adsorption thermodynamics and desorption properties of gaseous polycyclic aromatic hydrocarbons on mesoporous adsorbents. Adsorption. **23**, 361–371 (2017). https://doi.org/10.1007/s10450-017-9863-8
21. H. Li, X. He, T. Wu, B. Jin, L. Yang, J. Qiu, Synthesis, modification strategies and applications of coal-based carbon materials. Fuel Process. Technol. **230**, 107203 (2022). https://doi.org/10.1016/j.fuproc.2022.107203
22. X. Zhang, Y. Li, Z. Zhang, M. Nie, L. Wang, H. Zhang, Adsorption of condensable particulate matter from coal-fired flue gas by activated carbon. Sci. Total Environ. **778**, 146245 (2021). https://doi.org/10.1016/j.scitotenv.2021.146245
23. S. Wongcharee, V. Aravinthan, L. Erdei, W. Sanongraj, Use of macadamia nut shell residues as magnetic nanosorbents. Int. Biodeterior. Biodegrad. **124**, 276–287 (2017). https://doi.org/10.1016/j.ibiod.2017.04.004
24. X. Liu, J. Tian, Y. Li, N. Sun, S. Mi, Y. Xie, Z. Chen, Enhanced dyes adsorption from wastewater via Fe3O4 nanoparticles functionalized activated carbon. J. Hazard. Mater. **373**, 397–407 (2019). https://doi.org/10.1016/j.jhazmat.2019.03.103
25. M. Rani, U. Shanker, Metal oxide-chitosan based nanocomposites for efficient degradation of carcinogenic PAHs. J. Environ. Chem. Eng. **8**(3), 103810 (2020). https://doi.org/10.1016/j.jece.2020.103810
26. M. Lv, D. Li, Z. Zhang, B.E. Logan, G. Liu, M. Sun, C. Dai, Y. Feng, Unveiling the correlation of Fe3O4 fractions upon the adsorption behavior of sulfamethoxazole on magnetic activated carbon. Sci. Total Environ. **757**, 143717 (2021). https://doi.org/10.1016/j.scitotenv.2020.143717
27. A. Mehdinia, N. Khodaee, A. Jabbari, Fabrication of graphene/Fe3O4@ polythiophene nanocomposite and its application in the magnetic solid-phase extraction of polycyclic aromatic hydrocarbons from environmental water samples. Anal. Chim. Acta **868**, 1–9 (2015). https://doi.org/10.1016/j.aca.2014.12.022
28. M. Aghayi-Anaraki, V. Safarifard, Fe3O4@ MOF magnetic nanocomposites: synthesis and applications. Eur. J. Inorg. Chem. **2020**(20), 1916–1937 (2020). https://doi.org/10.1002/ejic.202000012
29. Y. Tian, Z. Xu, Z. Liu, X. Si, F. Zhang, W. Jiang, Fe3O4@ SiO2@ VAN nanoadsorbent followed by GC-MS for the determination of polycyclic aromatic hydrocarbons at ultra-trace levels in environmental water samples. Nanomaterials. **12**(17), 2921 (2022). https://doi.org/10.3390/nano12172921
30. H. Abdollahzadeh, M. Fazlzadeh, S. Afshin, H. Arfaeinia, A. Feizizadeh, Y. Poureshgh, Y. Rashtbari, Efficiency of activated carbon prepared from scrap tires magnetized by Fe3O4 nanoparticles: characterisation and its application for removal of reactive blue19 from aquatic solutions. Int. J. Environ. Anal. Chem. **102**(8), 1911–1925 (2022). https://doi.org/10.1080/03067319.2020.1745199
31. R. Foroutan, R. Mohammadi, A. Ahmadi, G. Bikhabar, F. Babaei, B. Ramavandi, Impact of ZnO and Fe3O4 magnetic nanoscale on the Methyl Violet 2B removal efficiency of the activated carbon oak wood. Chemosphere. **286**, 131632 (2022). https://doi.org/10.1016/j.chemosphere.2021.131632
32. S. Shewatatek, G. Gonfa, S. Mekuria, B. Tessema, G. Kezembayeva, K.S. Ghosh, M. Mushtaq, M.H. Diyanatizadeh, K. Isinkaralar, A. Hosseini-Bandegharaei, Synthesis of diatomite/Fe3O4/Teff straw activated carbon composite adsorbent for cr (VI) removal from wastewater. Results Chem. , 102486 (2025). https://doi.org/10.1016/j.rechem.2025.102486
33. G. Liu, N. Liu, H. Zhang, Z. Li-xi, The adsorption of arsenic on magnetic iron oxide in aqueous solutions. Desalination Water Treat. **21**, 96 (2010). https://doi.org/10.5004/dwt.2010.1253
34. R.B. Chesne, C.S. Kim, Zn(II) and Cu(II) adsorption and retention onto iron oxyhydroxide nanoparticles: effects of particle aggregation and salinity. Geochem. Trans. (2014). https://doi.org/10.1186/1467-4866-15-6
35. K. Mashale, T.M. Mogashane, P. Madzivha, M.A. Motlatle, L. Mokoena, J. Tshilongo, Iron Oxide and Hydroxides for the Removal of Heavy Metals from Wastewater. In IntechOpen eBooks (2025). IntechOpen. https://doi.org/10.5772/intechopen.1010016
36. S.S. Khasraw, D.M. Mamand, S.R. Saeed, A. Hassanzadeh, S.B. Aziz, O.G. Abdullah, Optoelectronic characteristics of PVA: Fe3O4 magnetic nanocomposite films. Int. J. Polym. Anal. Charact. 1–32 (2025). https://doi.org/10.1080/1023666X.2025.2506744
37. Y. Lv, J. Sun, G. Yu, W. Wang, Z. Song, X. Zhao, Y. Mao, Hydrophobic design of adsorbent for VOC removal in humid environment and quick regeneration by microwave. Microporous Mesoporous Mater. **294**, 109869 (2020). https://doi.org/10.1016/j.micromeso.2019.109869
38. K. Isinkaralar, Optimal preparation of low-cost activated carbon: the enhanced mechanism of interaction and performance studies for volatile organic compounds (VOCs) capture. Biomass Convers. Biorefin. **15**(3), 4371–4380 (2025). https://doi.org/10.1007/s13399-023-05159-9
39. I. Langmuir, The adsorption of gases on plane surfaces of glass, mica and platinum. J. Am. Chem. Soc. **40**(9), 1361–1403 (1918). https://doi.org/10.1021/ja02242a004
40. H. Freundlich, Über die adsorption in lösungen. Z. FÃ¼r Phys. Chem. **57**(1), 385–470 (1907). https://doi.org/10.1515/zpch-1907-5723
41. H. Moussout, H. Ahlafi, M. Aazza, H. Maghat, Critical of linear and nonlinear equations of pseudo-first order and pseudo-second order kinetic models. Karbala Int. J. Mod. Sci. **4**(2), 244–254 (2018). https://doi.org/10.1016/j.kijoms.2018.04.001
42. K. Suwannahong, S. Wongcharee, T. Kreetachat, S. Imman, N. Suriyachai, S. Hongthong, J. Rioyo, W. Dechapanya, P. Noiwimol, Comprehensive cost–benefit and statistical analysis of isotherm and kinetic models for heavy metal removal in acidic solutions using weakly base polymeric chelating resin as adsorbent. Water. **16**(17), 2384 (2024). https://doi.org/10.3390/w16172384
43. J.C. Bullen, S. Saleesongsom, K. Gallagher, D.J. Weiss, A revised pseudo-second-order kinetic model for adsorption, sensitive to changes in adsorbate and adsorbent concentrations. Langmuir. **37**(10), 3189–3201 (2021). https://doi.org/10.1021/acs.langmuir.1c00142
44. A. Savara, Standard states for adsorption on solid surfaces: 2D gases, surface liquids, and Langmuir adsorbates. J. Phys. Chem. C **117**(30), 15710–15715 (2013). https://doi.org/10.1021/jp404398z
45. A.L. Myers, P.A. Monson, Physical adsorption of gases: the case for absolute adsorption as the basis for thermodynamic analysis. Adsorption. **20**, 591–622 (2014). https://doi.org/10.1007/s10450-014-9604-1
46. S. Nikam, D. Mandal, Equilibrium and thermodynamic study of trichloroethylene adsorption on activated carbon in a fluidized bed and its thermal regeneration. Can. J. Chem. Eng. **101**(1), 451–462 (2023). https://doi.org/10.1002/cjce.24381
47. T. Jóźwiak, U. Filipkowska, A. Kowalkowska, J. Struk-Sokołowska, D. Werbowy, The influence of amination of sorbent based on buckwheat (*Fagopyrum esculentum*) husks on the sorption effectiveness of reactive black 5 dye. J. Environ. Chem. Eng. **9**(2), 105092 (2021). https://doi.org/10.1016/j.jece.2021.105092
48. J. Wang, C. Sun, Q.X. Huang, Y. Chi, J.H. Yan, Adsorption and thermal degradation of microplastics from aqueous solutions by Mg/Zn modified magnetic biochars. J. Hazard. Mater. **419**, 126486 (2021). https://doi.org/10.1016/j.jhazmat.2021.126486

49. C. Shi, S. Zhang, J. Zhao, J. Ma, H. Wu, H. Sun, S. Cheng, Experimental study on removal of microplastics from aqueous solution by magnetic force effect on the magnetic sepiolite. Sep. Purif. Technol. **288**, 120564 (2022). https://doi.org/10.1016/j.seppur.2022.120564
50. H. Li, M. Tang, J. Wang, L. Dong, L. Wang, Q. Liu, Q. Huang, S. Lu, Theoretical and experimental investigation on rapid and efficient adsorption characteristics of microplastics by magnetic sponge carbon. Sci. Total Environ. **897**, 165404 (2023). https://doi.org/10.1016/j.scitotenv.2023.165404
51. A.R. Bagheri, M. Ghaedi, A. Asfaram, A.A. Bazrafshan, R. Jannesar, Comparative study on ultrasonic assisted adsorption of dyes from single system onto Fe3O4 magnetite nanoparticles loaded on activated carbon: experimental design methodology. Ultrason. Sonochem. **34**, 294–304 (2017). https://doi.org/10.1016/j.ultsonch.2016.05.047
52. S. Park, C.J. Raj, R. Manikandan, B.C. Kim, K.H. Yu, Improved electrochemical performance of Fe3O4 nanoparticles decorated activated carbon supercapacitor electrodes. Bull. Korean Chem. Soc. **41**(8), 856–863 (2020). https://doi.org/10.1002/bkcs.12078
53. F. Gheitasi, S. Ghammamy, M. Zendehdel, F.B. Semiromi, Removal of mercury (II) from aqueous solution by powdered activated carbon nanoparticles prepared from beer barley husk modified with Thiol/Fe3O4. J. Mol. Struct. **1267**, 133555 (2022). https://doi.org/10.1016/j.molstruc.2022.133555
54. R.S. Juang, Y.C. Yei, C.S. Liao, K.S. Lin, H.C. Lu, S.F. Wang, A.C. Sun, Synthesis of magnetic Fe3O4/activated carbon nanocomposites with high surface area as recoverable adsorbents. J. Taiwan Inst. Chem. Eng. **90**, 51–60 (2018). https://doi.org/10.1016/j.jtice.2017.12.005
55. R. Vinayagam, S. Pai, G. Murugesan, T. Varadavenkatesan, K. Kaviyarasu, R. Selvaraj, Green synthesized hydroxyapatite nanoadsorbent for the adsorptive removal of AB113 dye for environmental applications. Environ. Res. **212**, 113274 (2022). https://doi.org/10.1016/j.envres.2022.113274
56. F. Guo, X. Jiang, X. Li, X. Jia, S. Liang, L. Qian, Synthesis of MgO/Fe3O4 nanoparticles embedded activated carbon from biomass for high-efficient adsorption of malachite green. Mater. Chem. Phys. **240**, 122240 (2020). https://doi.org/10.1016/j.matchemphys.2019.122240
57. T.J. Al-Musawi, G. McKay, A. Kadhim, M.M. Joybari, D. Balarak, Activated carbon prepared from hazelnut shell waste and magnetized by Fe3O4 nanoparticles for highly efficient adsorption of fluoride. Biomass Convers. Biorefin. **14**(4), 4687–4702 (2024). https://doi.org/10.1007/s13399-022-02593-z
58. A. Mohammadifard, D. Allouss, M. Vosoughi, A. Dargahi, A. Moharrami, Synthesis of magnetic Fe3O4/activated carbon prepared from banana peel (BPAC@ Fe3O4) and salvia seed (SSAC@ Fe3O4) and applications in the adsorption of basic blue 41 textile dye from aqueous solutions. Appl. Water Sci. **12**(5), 88 (2022). https://doi.org/10.1007/s13201-022-01622-6
59. K.K. Zadeh, D. Jafari, Activated carbon/alginate/Fe3O4 magnetic nanocomposite as a superior functional material for removal of lead from aqueous media. Biomass Convers. Biorefin. **14**(16), 19025 (2023). https://doi.org/10.1007/s13399-023-04040-z
60. H. El Harmoudi, L. El Gaini, E. Daoudi, M. Rhazi, Y. Boughaleb, M.A. El Mhammedi, A. Migalska-Zalas, M. Bakasse, Removal of 2, 4-D from aqueous solutions by adsorption processes using two biopolymers: chitin and chitosan and their optical properties. Opt. Mater. **36**(9), 1471–1477 (2014). https://doi.org/10.1016/j.optmat.2014.03.040
61. V.O. Njoku, M.A. Islam, M. Asif, B.H. Hameed, Utilization of Sky fruit husk agricultural waste to produce high quality activated carbon for the herbicide Bentazon adsorption. Chem. Eng. J. **251**, 183–191 (2014). https://doi.org/10.1016/j.cej.2014.04.015
62. M.H. Do, N.H. Phan, T.D. Nguyen, T.T.S. Pham, V.K. Nguyen, T.T.T. Vu, T.K.P. Nguyen, Activated carbon/Fe3O4 nanoparticle composite: fabrication, Methyl orange removal and regeneration by hydrogen peroxide. Chemosphere. **85**(8), 1269–1276 (2011). https://doi.org/10.1016/j.chemosphere.2011.07.023
63. M.N. Lincold, M.L. Jules, N.P. Guy, M. Suzanne, M.B. Jacques, T. Sylvain, V.O. Shikuku, G.P. Tchieta, Enhanced adsorption of malachite green onto a composite material activated carbon and iron (III) oxide nanoparticles: isotherm, kinetic, and thermodynamic study. Biomass Convers. Biorefinery. 1–20 (2024). https://doi.org/10.1007/s13399-024-06277-8
64. L. Liu, C. Yang, W. Tan, Y. Wang, Degradation of acid red 73 by activated persulfate in a heat/Fe3O4@ AC system with ultrasound intensification. ACS Omega **5**(23), 13739–13750 (2020). https://doi.org/10.1021/acsomega.0c00903
65. R. Cao, S. Liu, X. Yang, C. Wang, Y. Wang, W. Wang, Y. Pi, Enhanced remediation of cr (VI)-contaminated groundwater by coupling electrokinetics with ZVI/Fe3O4/AC-based permeable reactive barrier. J. Environ. Sci. **112**, 280–290 (2022). https://doi.org/10.1016/j.jes.2021.05.002
66. B. Kakavandi, R.R. Kalantary, A.J. Jafari, S. Nasseri, A. Ameri, A. Esrafili, A. Azari, Pb (II) adsorption onto a magnetic composite of activated carbon and superparamagnetic Fe3O4 nanoparticles: experimental and modeling study. CLEAN Soil Air Water **43**(8), 1157–1166 (2015). https://doi.org/10.1002/clen.201400568
67. R. Foroutan, S.J. Peighambardoust, S.H. Peighambardoust, M. Pateiro, J.M. Lorenzo, Adsorption of crystal violet dye using activated carbon of lemon wood and activated carbon/Fe3O4 magnetic nanocomposite from aqueous solutions: a kinetic, equilibrium and thermodynamic study. Molecules **26**(8), 2241 (2021). https://doi.org/10.3390/molecules26082241
68. S. Joshi, V.K. Garg, N. Kataria, K. Kadirvelu, Applications of Fe3O4@ AC nanoparticles for dye removal from simulated wastewater. Chemosphere. **236**, 124280 (2019). https://doi.org/10.1016/j.chemosphere.2019.07.011
69. H. Khaleghi, H. Esmaeili, N. Jaafarzadeh, B. Ramavandi, Date seed activated carbon decorated with CaO and Fe3O4 nanoparticles as a reusable sorbent for removal of formaldehyde. Korean J. Chem. Eng. **39**(1), 146–160 (2022). https://doi.org/10.1007/s11814-021-0972-4
70. Z. Duan, W. Zhang, M. Lu, Z. Shao, W. Huang, J. Li, Y. Li, J. Mo, Y. Li, C. Chen, Magnetic Fe3O4/activated carbon for combined adsorption and Fenton oxidation of 4-chlorophenol. Carbon. **167**, 351–363 (2020). https://doi.org/10.1016/j.carbon.2020.05.106
71. M. Orrantia, M.A. Armenta, L.H. Alvarez, V.A. Burboa-Charis, E.R. Meza-Escalante, A. Olivas, E. Arroyo, V.M. Maytorena, Enhanced methane production via anaerobic digestion assisted with Fe3O4 nanoparticles supported on microporous granular activated carbon. Fuel. **360**, 130517 (2024). https://doi.org/10.1016/j.fuel.2023.130517
72. U. Herrera-García, J. Castillo, D. Patiño-Ruiz, R. Solano, A. Herrera, Activated carbon from Yam peels modified with Fe3O4 for removal of 2, 4-dichlorophenoxyacetic acid in aqueous solution. Water. **11**(11), 2342 (2019). https://doi.org/10.3390/w11112342
73. E. Mirzaee, M. Sartaj, Synthesis and evaluation of recoverable activated carbon/Fe3O4 composites for removal of polycyclic aromatic hydrocarbons from aqueous solution. Environ. Technol. Innov. **25**, 102174 (2022). https://doi.org/10.1016/j.eti.2021.102174
74. C. Carlini, S. Chaudhuri, O. Mann, D. Tomsik, T. Hüffer, N. Greggio, D. Marazza, T. Hofmann, G. Sigmund, Benchmarking biochar with activated carbon for immobilizing leachable PAH and heterocyclic PAH in contaminated soils. Environ. Pollut. **325**, 121417 (2023). https://doi.org/10.1016/j.envpol.2023.121417

75. K. Rambabu, G. Bharath, F. Banat, P.L. Show, Green synthesis of zinc oxide nanoparticles using *Phoenix dactylifera* waste as bioreductant for effective dye degradation and antibacterial performance in wastewater treatment. J. Hazard. Mater. **402**, 123560 (2021). https://doi.org/10.1016/j.jhazmat.2020.123560
76. B.V. Babu, S. Gupta, Adsorption of cr (VI) using activated neem leaves: kinetic studies. Adsorption **14**(1), 85–92 (2008). https://doi.org/10.1007/s10450-007-9057-x
77. M.Y. Badi, A. Azari, H. Pasalari, A. Esrafili, M. Farzadkia, Modification of activated carbon with magnetic Fe3O4 nanoparticle composite for removal of ceftriaxone from aquatic solutions. J. Mol. Liq. **261**, 146–154 (2018). https://doi.org/10.1016/j.molliq.2018.04.019
78. P. Aungthitipan, A. Janthakhot, P. Tansomrot, S. Wongcharee, S. Hongthong, T. Kreetachat, S. Imman, W. Dechapanya, Mesoporous biochar composite derived from hardwood and post-recycled plastic waste in Thailand: a case study of nickel removal in acidic solution. S. Afr. J. Chem. Eng. (2025). https://doi.org/10.1016/j.sajce.2025.05.002
79. P. Tansomros, P. Aungthitipan, S. Wongcharee, S. Hongthong, T. Kreetachat, N. Suriyachai, W. Dechapanya, N. Papukdee, C. Jareanpon, Evaluating and selecting kinetic and isotherm models for copper and nickel removal using cow bone char as an adsorbent via excel solver functions. Int. J. Mol. Sci. **26**(9), 4316 (2025). https://doi.org/10.3390/ijms26094316